

Local insulator-to-superconductor transition in amorphous InO_x films modulated by e-beam irradiation

Iago F. Llovo^{1,2,3,*} and Julien Delahaye^{4,†}

¹Centro de Supercomputación de Galicia (CESGA), 15705 Santiago de Compostela, Spain

²QMatterPhotonics, Departamento de Física de Partículas, Universidade de Santiago de Compostela, 15782 Santiago de Compostela, Spain

³iMATUS, Universidade de Santiago de Compostela, 15782 Santiago de Compostela, Spain

⁴Univ. Grenoble Alpes, CNRS, Grenoble INP, Institut Néel, 38000 Grenoble, France

ABSTRACT

We present a novel method enabling precise post-fabrication modulation of the electrical resistance in micrometer-scale regions of amorphous indium oxide (a-InO_x) films. By subjecting initially insulating films to an electron beam at room temperature, we demonstrate that the exposed region of the films becomes superconducting. The resultant superconducting transition temperature (T_c) is adjustable up to 2.8 K by changing the electron dose and accelerating voltage. This technique offers a compelling alternative to traditional a-InO_x annealing methods for both fundamental investigations and practical applications. Moreover, it empowers independent adjustment of electrical properties across initially identical a-InO_x samples on the same substrate, facilitating the creation of superconducting microstructures with precise T_c control at the micrometer scale. Some possible mechanisms for the observed resistance modifications are discussed.

Introduction

Disordered amorphous indium oxide (a-InO_x) films have long served as an experimental platform for studying the electrical properties of disordered systems. During the 1980s, many theoretical predictions related to the Mott-Anderson metal-insulator transition were verified in this system [1, 2, 3] and in the early 1990s, two new topics rose from disordered indium oxide films measurements. The first topic was the search for an electron glass [4, 5, 6], with the reports of slow and glassy relaxations of the conductance in field effect experiments on insulating films [7, 8, 9]. The second topic was the study of the superconducting-insulator transition (SIT) in amorphous films as a function of magnetic field [10, 11, 12] and disorder [13]. The nature of this transition, especially the insulating state terminating superconductivity, remain the subject of heated experimental and theoretical debates [14, 15]. The unusual properties of this insulating state may indeed reflect the existence of a many body localized phase [16], a topical and striking issue in condensed matter physics [17, 18, 19, 20, 21].

From an applications perspective, a-InO_x films are also a promising system for the fabrication of high kinetic inductances. Such electrical circuit elements can be obtained from superconducting a-InO_x films approaching the SIT, in the form of long wires of a few micrometers wide [22, 23] from which low-loss and small size microwave resonators can be made, crucial for the development of quantum circuits [15, 22, 23]. Additionally, these films have been used to manufacture sensitive kinetic inductance photon detectors [24]. Doped a-InO_x films have also found extensive use in the production of semiconducting microdevices, such as transparent thin-film transistors (TFT). As oxygen-vacancies in a-InO_x exhibit electronic properties equivalent to those of tin-doped amorphous indium-tin oxide (a-ITO) [25], fields already benefiting from the commercial use of a-ITO (e.g., transparent display research) could also potentially leverage the control of the electronic properties of a-InO_x .

The prospects for fundamental studies and applications of a-InO_x rely on the ability to control and adjust the electrical properties of these films, which exhibit significant variability across the SIT. These films are typically prepared by sputtering or electron beam (e-beam) deposition of pure In_2O_3 under a partial pressure of oxygen [3, 26, 27, 28, 29, 30]. Oxygen vacancies are created during deposition, so the stoichiometric composition of the amorphous film is less oxygen-rich than the In_2O_3 target, and can be regulated by the relative oxygen pressure during deposition [31]. Additionally, the deposition conditions can also affect the crystallinity of the thin films: microcrystalline films result from evaporation at substrate temperatures exceeding

* ifllovo@cesga.es (Corresponding author)

† julien.delahaye@neel.cnrs.fr

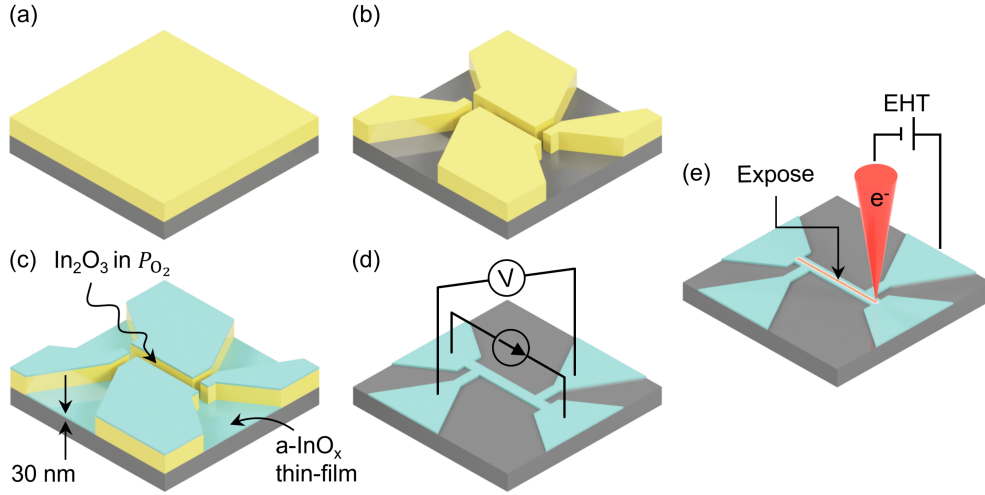


Figure 1. (a) A negative PMMA resist mask (yellow) was deposited on highly-doped Si substrates coated with 100 nm of thermally grown SiO₂ and (b) patterned using standard EBL. (c) a-InO_x thin films (cyan) were then deposited in an oxygen-controlled atmosphere to obtain samples close to the SIT. (d) After lift-off, the pristine samples evolved at room temperature for over a day and were characterized by measuring the $R(T)$ curves down to ~ 1.6 K. (e) Controlled e-beam exposure to pattern microstructures on the InO_x channels resulted in increased conductivity, eventually crossing the SIT.

150°C, while substrate temperatures below 40°C yield amorphous films [3]. Therefore, common methods for adjusting the electrical properties of the resulting films include adjusting the oxygen pressure, the evaporation rate or the film thickness during the evaporation process, and employing post-evaporation annealing [13, 32]. In the case of amorphous films, annealing steps restricted to 40–60°C lead to irreversible reductions in electrical resistance without inducing crystallization [3, 13].

In this article, we introduce a novel technique for modulating the electrical properties of a-InO_x films in relation to the SIT. We demonstrate that upon exposure to the e-beam of a scanning electron microscope (SEM), an initially insulating film undergoes a local transformation into the superconducting phase across the SIT, featuring a superconducting transition temperature of up to 2.8 K. Moreover, we demonstrate the capability of controlled e-beam exposure to locally manipulate the SIT, achieving a lateral resolution of a few micrometers. Finally, we discuss the potential origins of these alterations and the opportunities afforded by this new technique.

Methods

Sample deposition

The sample fabrication and treatment procedures are illustrated in Fig. 1. Firstly, the insulating a-InO_x films were manufactured via e-beam evaporation. A resist mask was first made using standard e-beam lithography (EBL) on highly-doped Si substrates coated with 100 nm of thermally grown SiO₂. Subsequently, pure In₂O₃ was e-beam evaporated and deposited on the masked substrates at a rate of 2 Å/s under a partial O₂ pressure. The evaporation was stopped after depositing 30 nm on the substrate. A precise O₂ pressure of $3.0 - 3.1 \times 10^{-5}$ mbar (with base pressure of the evaporator at 10^{-6} mbar) was selected through trial-and-error to ensure that the samples were in the regime of interest, close to the SIT transition, yet retaining insulating behavior down to temperatures of $\simeq 1.7$ K. Finally, the resist mask was removed using acetone (lift-off). Up to 20 samples were made for each batch, on a single 1 cm \times 1 cm substrate. Different geometries were tested, with channel width (W) \times length (L) ranging 5 – 10 μm \times 20 – 25 μm , except for certain samples designed as long wires (1 μm \times 25 μm , see Table 1). No external heating or cooling of the substrate was applied throughout these fabrication steps (evaporation and lift-off).

$R_{\square} - T$ characterization

Following sample deposition, the DC electrical resistance R of the samples was measured with a 4-contact method using a Keithley 6221 current source and a Keithley 2182A nanovoltmeter. The sheet resistance of the samples $R_{\square} = R \cdot L/W$ was then obtained from the actual geometric factor L/W of samples, calculated from optical microscopy images. In the R_{\square} range of our films (around 3 k Ω at room temperature), a small resistance drift was observed, well described by a $\log(t)$ decrease, where t is the time elapsed at room temperature after deposition. To mitigate the effects of this drift, the samples were left at room temperature for at least one day after lift-off, prior to low temperature characterization and subsequent e-beam treatment.

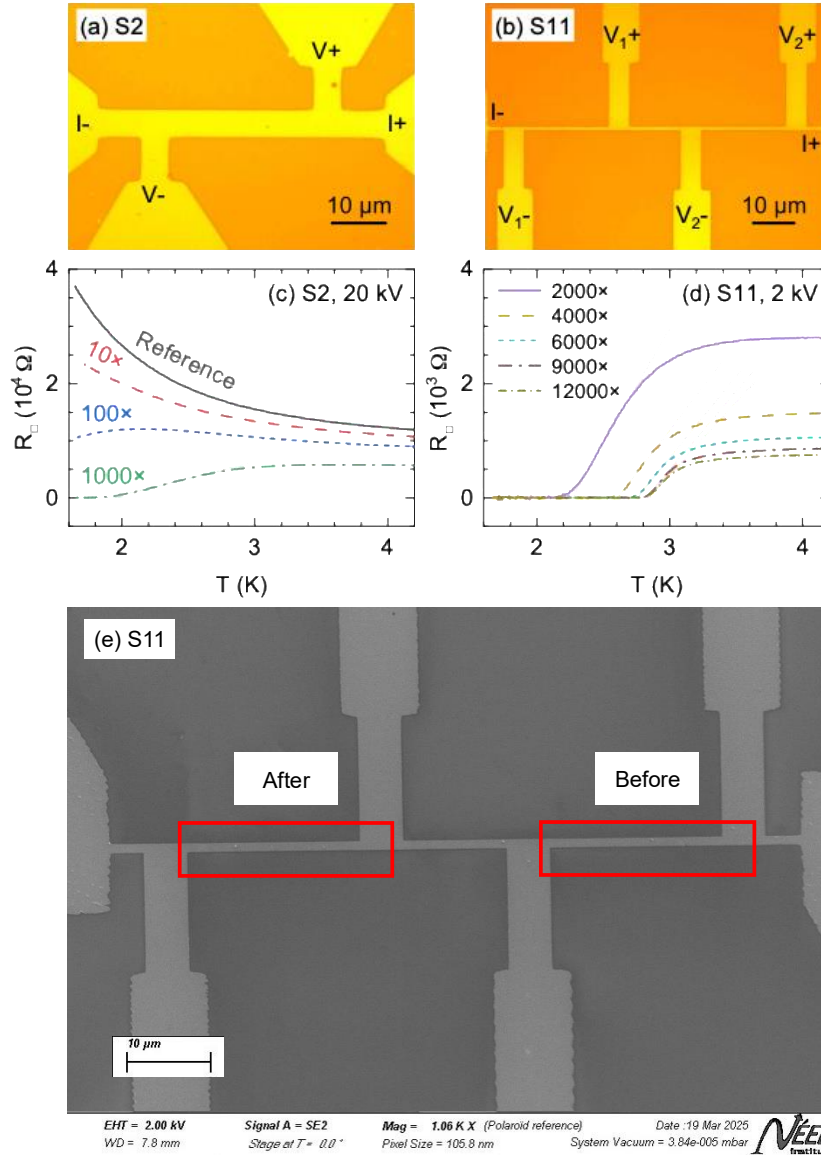


Figure 2. (a, b) Geometry of two channels from substrates S2 and S11, and (c, d) their corresponding $R_{\square}(T)$ curves before (reference) and after the e-beam treatment. Doses are indicated as multiples of the standard dose for PMMA resist, $250 \mu\text{C cm}^{-2}$. A 20 kV e-beam was used to expose samples on substrate S2, finding a progressive evolution with dose, from insulating to superconducting behavior. With a dose of 1000 \times , the sample became superconducting below 1.9 K. A 2 kV e-beam at higher doses was used to expose samples on S11. All the channels of sample S11 became superconducting after the treatment, with a progressive increase of T_c with dose, from 2.28 K up to 2.84 K, and a diminution of the normal state sheet resistance from 12 k Ω at 4.2 K (reference sample, not shown) down to less than 1 k Ω for a dose of 12000 \times . This anticorrelation of normal state resistivity and T_c is also present in a-InO $_x$ samples made by tuning the O $_2$ pressure during deposition. (e) SEM micrograph of S11, where the left channel had been previously treated (12000 \times dose) and the right one was kept pristine until before the capture. No morphological changes could be observed between untreated and treated channels by visual inspection.

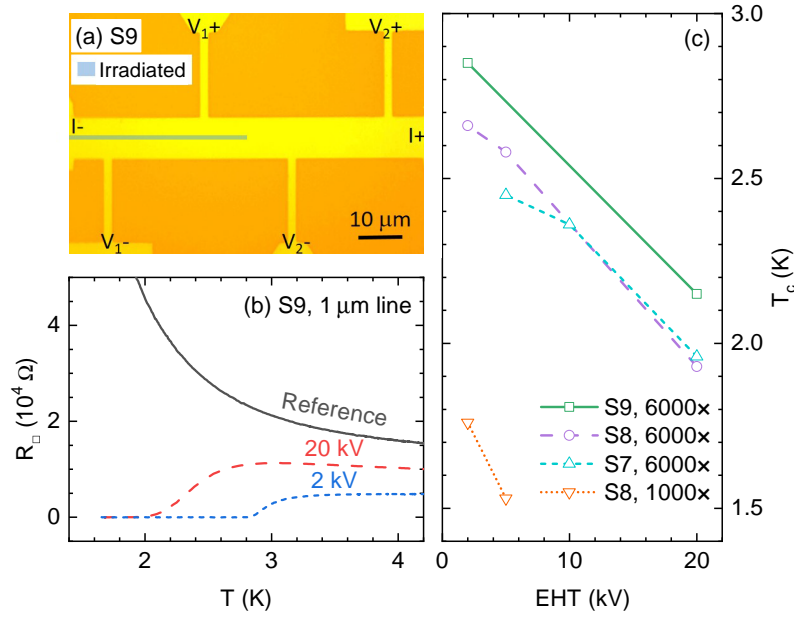


Figure 3. Results of the e-beam treatment with different acceleration voltages. (a) Diagram of the irradiated area, a 1 μm wide line in the middle of the a-InO_x channel, represented as the shaded area on top of the optical microscope image. (b) $R_{\square}(T)$ curves measured for substrate S9 before (reference, solid black line) and after the treatment. A clear T_c increase was observed when the acceleration voltage of the electrons was reduced from 20 kV (long-dashed red line, $T_c = 2.0$ K) to 2 kV (short-dashed blue line, $T_c = 2.8$ K). (c) Evolution of T_c with the acceleration voltage EHT for three different samples.

After one day, the relative variations in resistance were less than 1% over the following day. The samples were then cooled and measured down to 1.6 – 1.7 K in a Variable Temperature Insert (VTI), in order to verify their insulating nature. For each sample, sufficiently low currents were selected to prevent self-heating while maintaining a high signal-to-noise ratio. A custom-made voltage preamp was occasionally employed to reduce the noise level of the most resistive samples.

Our deposition setup facilitated the achievement of high sample-to-sample repeatability (within the same batch deposited on a single 1 cm \times 1 cm substrate) of both the geometrical factors of the a-InO_x channel and their sheet resistance at both room temperature and 4.2 K, with the exception of the long wires, for which the geometrical factors were less accurately determined during development. However, the batch-to-batch variation of R_{\square} was between 2.7 and 3.7 k Ω at 295 K; 12 and 22 k Ω at 4.2 K; and 40 k Ω and 200 k Ω at 1.7 K (with 10 different evaporation runs conducted), despite maintaining identical nominal evaporation parameters (oxygen pressure and evaporation rate). This highlights the challenge of finely controlling the electrical properties of the a-InO_x films solely through e-beam evaporation.

Sample treatment

Following the initial characterization, the 1 cm \times 1 cm substrates were transferred into the chamber of a LEO1530 scanning electron microscope, where they underwent exposure to the e-beam using a standard lithography controller and software (RAITH Elphy Plus). This system offers flexibility in adjusting both the acceleration voltage of the electron beam and the electron dose per surface area received by the samples, while also enabling precise control over which part of the channel is exposed (as detailed below). A reference sample from each substrate was kept unexposed throughout the experiments. This reference sample served to monitor any potential resistance drift at room temperature and to investigate possible spurious effects that could induce annealing. Subsequently, the samples were reinstalled in the VTI, and resistance-versus-temperature curves for both the e-beam-exposed and reference channels were measured and compared. No significant effects were observed on the reference samples following the exposure of the samples of the same batch, except for the natural evolution of a-InO_x film properties due to the brief periods of time during which the samples remained at room temperature. As shown in Fig. 2(e), no morphological changes could be observed between untreated and treated channels in SEM micrographs.

Results

Our main contribution is the proposal of a novel technique for local modulation of the electronic properties of a-InO_x films across the superconductor-insulator transition through prolonged exposure to an e-beam. As shown in Fig. 2, the R_{\square} versus T curves

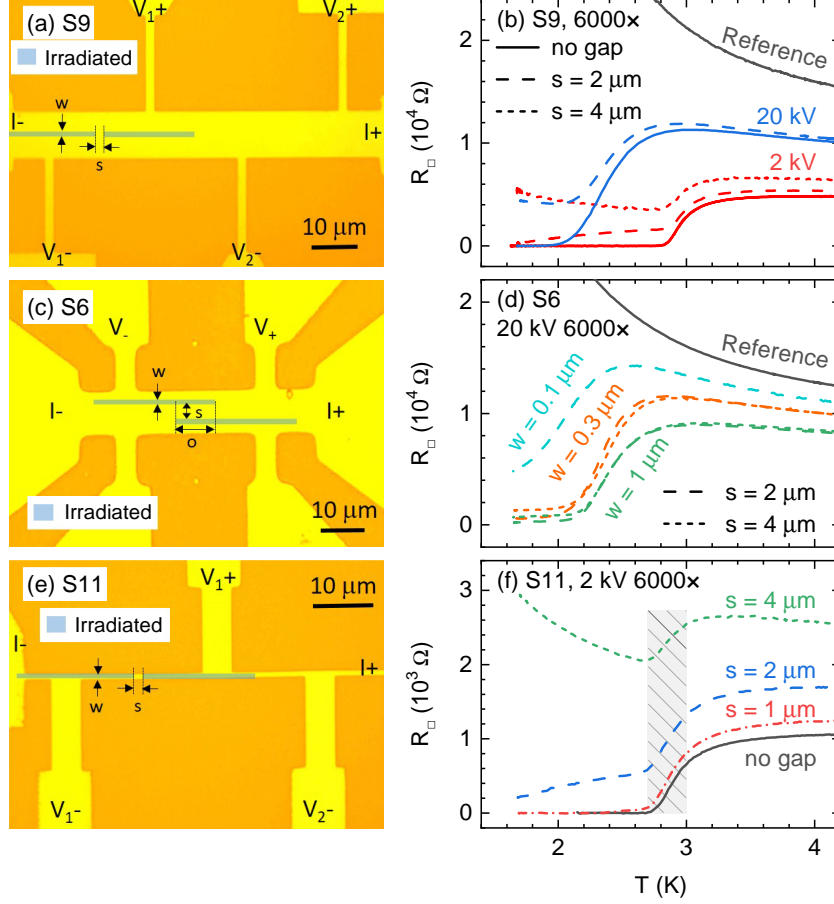


Figure 4. The spatial resolution of the e-beam treatment was tested using different acceleration voltages and geometries, and with a dose of 6000×, almost sufficient to saturate the T_c value (see Fig. 2 (d)). (a, b) 1 μm wide lines, embedded in an insulating matrix, and separated by an insulating gap of length s , were drawn on substrate S9 at both 2 kV and 20 kV. (c, d) On substrate S6, lines of different width w , overlapping 10 μm longitudinally and separated by a distance s transversally were drawn instead. (e, f) Substrate S11 was finally used to draw 1 μm wide fully superconducting channels separated by an insulating gap of length s . As shown, fully superconducting behavior (i.e., $R = 0$) was not observed above 1.6 K for $s \geq 2 \mu\text{m}$, and the gap remained insulating for $s \geq 4 \mu\text{m}$. Nevertheless, the superconducting transition of the exposed part remained visible in all samples, evidencing the characteristic sudden resistance drop at a remarkably repeatable T_c within the same batch [see e.g. the shaded area in (f), with the exception of the 100 nm lines in (d)].

demonstrate an evolution with increased dose (expressed as a multiple of the standard dose for PMMA resist, $250 \mu\text{C cm}^{-2}$), from insulating ($dR/dT < 0$ at low T) to metallic ($dR/dT > 0$) and even superconducting behavior ($R_{\square} = 0$) at sufficiently low temperatures. Defining T_c from the linear extrapolation to $R = 0$ of the $R(T)$ curve at the point of maximum slope of the superconducting transition, a saturation value of $T_c \simeq 2.85 \text{ K}$ was achieved with error on the reported T_c below 0.05 K. For samples with gaps, the T_c values were estimated by setting the zero of resistivity at the minimum resistivity measured. The evolution towards the superconducting state and the increase of T_c are accompanied by a decrease of the normal state resistivity with the applied dose. Table 1 compiles all the treatments performed on different samples.

Given this result, we tested the possibility of drawing superconducting microstructures within an insulating a-InO_x matrix. We exposed lines measuring 1 μm wide within 5 – 10 μm wide channels (see Fig. 3 (a)). A zero-resistance state was observed at sufficiently low temperatures, evidencing the presence of a continuous line of superconducting material in the channel. The effect of the acceleration voltage on T_c is clearly discernible: for S9 (Fig. 3 (b), and squares and solid green line in (c)), we observed a T_c increase from 2.1 K up to 2.84 K as the acceleration voltage was decreased from 20 to 2 kV. This trend was consistently observed across different samples, as shown in Fig. 3 (c). A rough estimate of the effective e-beam-treated line width can be obtained from a comparison of the R_{\square} values in the normal state ($T \simeq 4.2 \text{ K}$) before and after the e-beam treatment. For a 1 μm wide line exposed in a 10 μm wide channel (corresponding to S9), R_{\square} decreased from 15 kΩ to 5 kΩ. In other

	V (kV)	I (nA)	Dose ($\times 250 \mu\text{C}/\text{cm}^2$)	Channel Size ($\mu\text{m} \times \mu\text{m}$)	Exposed Size (see main text)	T_c (K)	Notes
S2	20	1.04	10 \times	5 \times 25	Whole channel		Fig. 2(a, c)
	20	1.04	100 \times	5 \times 25	Whole channel	< 1.6	
	20	4.2	1000 \times	5 \times 25	Whole channel	1.9	
S5	20	4.16	6000 \times	10 \times 25	w=1 μm	2.65	ΔT discussion
	20	1.03	6000 \times	10 \times 25	w=1 μm	2.55	
S6	20	4.16	6000 \times	10 \times 25	w=1 μm , s=2 μm , o=10 μm	$\lesssim 2.21$	Fig. 4(c, d)
	20	4.16	6000 \times	10 \times 25	w=0.3 μm , s=2 μm , o=10 μm	$\lesssim 2.16$	
	20	1.03	6000 \times	10 \times 25	w=0.1 μm , s=2 μm , o=10 μm	$\lesssim 1.80$	
	20	4.16	6000 \times	10 \times 25	w=1 μm , s=4 μm , o=10 μm	$\lesssim 2.21$	
	20	4.16	6000 \times	10 \times 25	w=0.3 μm , s=4 μm , o=10 μm	$\lesssim 2.13$	
S7	20	3.62	6000 \times	10 \times 25	w=1 μm	1.96	Fig. 3c
	10	2.31	6000 \times	10 \times 25	w=1 μm	2.36	
	5	1.74	6000 \times	10 \times 25	w=1 μm	2.45	
S8	20	3.43	6000 \times	10 \times 20	w=1 μm	1.93	Fig. 3c
	5	1.65	6000 \times	10 \times 20	w=1 μm	2.58	
	2	1.32	6000 \times	10 \times 20	w=1 μm	2.66	
	5	1.65	1000 \times	10 \times 20	w=1 μm	1.53	
	2	1.32	1000 \times	10 \times 20	w=1 μm	1.76	
S9	20	3.43	6000 \times	10 \times 20	w=1 μm	2.10	Fig. 3 (a – c) , Fig. 4 (a, b)
	2	1.31	6000 \times	10 \times 20	w=1 μm	2.84	
	20	3.75	6000 \times	10 \times 20	w=1 μm , s=2 μm	$\lesssim 2.14$	
	2	1.46	6000 \times	10 \times 20	w=1 μm , s=2 μm	$\lesssim 2.85$	
	2	1.46	6000 \times	10 \times 20	w=1 μm , s=4 μm	$\lesssim 2.85$	
S11	2	1.48	2000 \times	1 \times 20	Whole channel	2.28	Fig. 2 (b, d) , Fig. 4 (e, f)
	2	1.48	4000 \times	1 \times 20	Whole channel	2.60	
	2	1.48	6000 \times	1 \times 20	Whole channel	2.74	
	2	1.48	9000 \times	1 \times 20	Whole channel	2.83	
	2	1.48	12000 \times	1 \times 20	Whole channel	2.84	
	2	1.48	6000 \times	1 \times 20	s=1 μm	2.71	
	2	1.48	6000 \times	1 \times 20	s=2 μm	$\lesssim 2.71$	
	2	1.48	6000 \times	1 \times 20	s=4 μm	$\lesssim 2.72$	

Table 1. E-beam treatments performed on the samples of this study. For samples with gaps, the T_c values were estimated by setting the zero of resistivity at the minimum resistivity measured.

samples where the whole channel was exposed, R_{\square} was approximately $\simeq 1 \text{ k}\Omega$ for similar e-beam parameters (acceleration voltage of 2 kV and dose factor of 6000 \times). Assuming that the measured resistance results from a parallel conduction between a homogeneous line affected by the e-beam and the rest of the channel, which remains unaffected, we infer that the effective line width is approximately $\sim 1.4 \mu\text{m}$, significantly larger than the nominal width.

Other microstructures were drawn to estimate the spatial resolution of the e-beam treatment. For instance, a single line of width w much narrower than the total channel width was exposed while leaving a length s unexposed in the center of the wire, creating an insulating interruption or “gap”, as shown in Fig. 4 (a). Another geometry consisted in exposing two parallel wires offset by a distance s , but longitudinally overlapping by a distance o , as shown in Fig. 4 (c). Additionally, in samples shaped as long, thin wires, the entire channel width could be exposed at high doses while leaving a small insulating gap s embedded in a fully superconducting wire, as pictured in Fig. 4 (e). The results of these tests were unequivocal – we successfully created short insulating interruptions within the superconducting exposed sections, as evidenced by the $R_{\square}(T)$ curves shown in Fig. 4 (b, d, f). At lower temperatures than the clearly visible superconducting transition of the exposed parts, an insulating behavior ($dR/dT < 0$) was observed down to $s \gtrsim 4 \mu\text{m}$. For gaps below this value, the wires become either

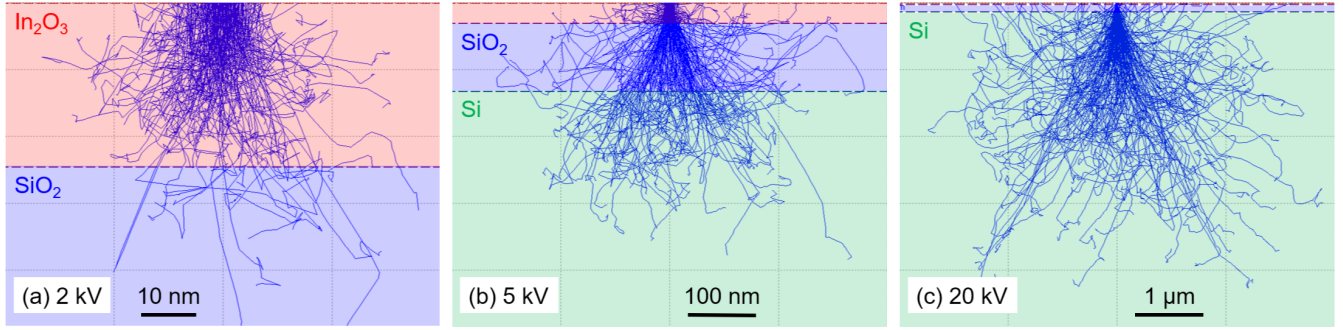


Figure 5. Simulations of the e-beam electron trajectories at different acceleration voltages: (a) 2 kV; (b) 5 kV; (c) 20 kV. The simulations were done using CASINO [38], and assuming 30 nm of In_2O_3 (red), 100 nm of SiO_2 (blue) and 10 μm of Si (green).

metallic ($dR/dT > 0$) or superconducting. This indicates that the resolution of our treatment is about $\sim 2 \mu\text{m}$, half the size of the gap. A spatial resolution of this order of magnitude was observed for all acceleration voltages. Finally, for one of the batches (S6), we investigated the effect of reducing line widths by adopting the second geometry and employing $w = (100 \text{ nm}, 300 \text{ nm}, 1 \mu\text{m})$. In this case, we observed very similar T_c and resolution length scale for $w = 300 \text{ nm}$ and $1 \mu\text{m}$, while a smaller T_c was obtained for $w = 100 \text{ nm}$ (see Fig. 4 d).

Discussion

We will now discuss the mechanisms that could explain the observed drop in electrical resistance after e-beam exposure. A standard process for tuning amorphous InO_x film resistance across the SIT is annealing [12, 13]. Below $\simeq 100^\circ\text{C}$, annealing induces an irreversible decrease in resistance while preserving the amorphous structure of the films [3], and is accompanied by a densification of the film [33, 34] while the charge carrier density remains essentially unchanged [12, 13]. In films with low carrier density ($n \simeq 10^{20} \text{ cm}^{-3}$), which exhibit high resistance in their non-annealed state [35], the resistance drop at room temperature can be of several orders of magnitude [35]. However, in our amorphous films, which are less resistive and have higher charge carrier density (according to our e-beam evaporation parameters – evaporation rate of 2 \AA/s and $P_{\text{O}_2} = 3 \times 10^{-5} \text{ mbar}$, $n \sim 10^{22} \text{ cm}^{-3}$), annealing may decrease the room temperature resistance by at most a factor of 4 [34]. Remarkably, this decrease is commensurate with the decrease observed at room temperature between the resistance of an unexposed film, and the same film exposed to the highest doses ($12000\times$). For example, in S11, R_{\square} decreases from $2.6 \text{ k}\Omega$ prior to e-beam exposure to $0.6 \text{ k}\Omega$ after (note that the relative changes at 4.2 K are larger: from $15 \text{ k}\Omega$ to $0.7 \text{ k}\Omega$). Hence, the question arises as to whether the SEM e-beam can induce such annealing. When the electron probe diameter is much smaller than the electron range λ in a solid, which seems reasonable in our case (see simulations below), an estimate of the local temperature increase ΔT is given by [36]

$$\Delta T = 3fUI/(2\pi\kappa\lambda). \quad (1)$$

In Eq. 1, f is the power conversion factor to heat, U the acceleration voltage of the electrons, I the current intensity of the e-beam, λ the electron range and κ the thermal conductivity of the material. Taking $f = 100\%$, $U = 20 \text{ kV}$, $I = 4 \text{ nA}$, $\lambda \simeq 1 \mu\text{m}$ and $\kappa \simeq 100 \text{ W m}^{-1} \text{ K}^{-1}$ (for Si^{++} substrate), we obtain $\Delta T \simeq 0.4^\circ\text{C}$. Taking the values for $U = 2 \text{ kV}$, $I = 1.5 \text{ nA}$ and $\lambda = 10 \text{ nm}$ instead, we obtain $\Delta T \simeq 1.5 \text{ K}$. These values are significantly smaller than the ΔT required for annealing of amorphous InO_x , which is typically several tens of degrees. It is worth noting that much larger ΔT over 1000 K have been reported [37] when using higher voltages in highly focused TEM (200 kV) or higher currents in a 40 kV SEM ($\sim 10 \text{ mA}$), while for similar voltages and doses using a SEM in similar conditions, the ΔT observed is in any case below 5 K . To evaluate the significance of an e-beam heating effect, we conducted experiments comparing resistance changes obtained under 20 kV but using two different currents and the same dose: 4.2 nA ($120 \mu\text{m}$ diaphragm) and 1.0 nA ($60 \mu\text{m}$ diaphragm). Minute R_{\square} and T_c changes were observed: R_{\square} at room temperature increased from $2.25 \text{ k}\Omega$ to $2.28 \text{ k}\Omega$, and T_c decreased from 2.65 K to 2.55 K .

The simulations of the electron trajectories at different acceleration voltages can provide insight into the potential mechanisms underlying the observed resistance changes. To conduct these simulations, we used CASINO Monte-Carlo software [38] and considered a structure comprising 30 nm of In_2O_3 , 100 nm of SiO_2 , and $10 \mu\text{m}$ of Si. From the results, illustrated in Fig. 5, we conclude that, at 20 kV , the electron range extends to a few micrometers within the Si substrate, whereas at 2 kV it remains confined within the 30 nm layer of a- InO_x . However, the part of the a- InO_x film directly affected by primary (and thus secondary) electrons is confined to a few tens of nanometers radially from the electron beam (assumed to have a diameter

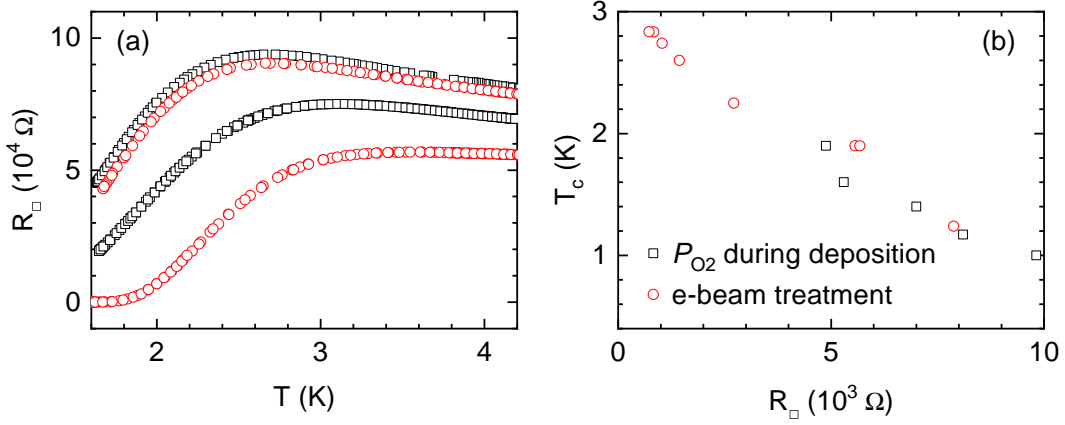


Figure 6. Comparison between samples manufactured using the standard method (changing P_{O_2} during deposition, black squares) and the technique proposed in this paper (red circles). (a) R_{\square} versus T curves between 1.7 K and 4.2 K for samples obtained using the standard method (upper curve: 40 nm thick, $P_{O_2} = 3 \times 10^{-5}$ mbar; lower curve: 30 nm, no O_2) and samples from this paper. (b) T_c versus R_{\square} at 4.2 K for samples obtained using the standard method (in ascending order of T_c : 20 nm, no O_2 ; 40 nm, $P_{O_2} = 3 \times 10^{-5}$ mbar; 30 nm, no O_2 ; 70 nm, $P_{O_2} = 3.8 \times 10^{-5}$ mbar; 47 nm, $P_{O_2} = 3.5 \times 10^{-5}$ mbar) and samples from this paper.

of 10 nm). Given that the region with reduced resistance due to the e-beam treatment extends approximately 1 μm beyond the exposed area, direct action of the e-beam electrons such as an e-beam-induced chemical reduction, previously reported in vanadium and titanium oxides [39, 40, 41, 42], cannot explain the observed changes. Nevertheless, the effect of UV exposure on indium oxide electrical resistance is well established. A conducting state was found in previous work on UV exposure in amorphous InO_x films, observing significant resistance changes which were attributed to a UV-photoreduction mechanism, where the conducting photoreduced state was found to be unstable in oxidizing atmosphere; subsequent ozone or O_2 plasma exposure of the films achieved the opposite effect, reverting the samples to the high resistance state [26, 27, 28, 29]. These photoreduction-oxidation cycles were associated with significant changes in the oxygen content of the topmost 10 nm layer of the film, and correlated with oxygen outdiffusion from the film [29]. Recent work by Lo Mastro et al. [43] studied the ageing of In_2O_3 films after different treatments to increase its carrier density, such as ion implantation and UV photoreduction, concluding that “*UV photo-reduction, both in argon saturated atmosphere or in air, is a simpler and very effective tool to induce intrinsic doping by formation of oxygen vacancies.*”. In our case, a fraction of the radiation emitted during electron-matter interactions in pear-shaped volume of interaction (see simulations) extends into the UV range, as the continuous X-ray spectrum reaches down to visible and near-UV energies [36]. In addition, cathodoluminescence may contribute as another UV source: nanocrystalline indium oxide and indium tin oxide films show a cathodoluminescence peak in the visible, extending into the near-UV [44, 45]. Although our films are amorphous rather than nanocrystalline, the underlying mechanism attributed to these emissions – transitions between shallow energy levels associated with point defects – could also play a role. While the exact microscopic origin of the resistance decrease remains to be established, these considerations indicate that indirect radiative processes are a plausible contributor to the observed behaviour.

Additional tests were conducted to evaluate the stability of the low resistance state obtained after e-beam exposure. A superconducting channel (with T_c around 2 K) was exposed to ambient air at room temperature for 3.5 days. A small resistance increase of the exposed channel from 2.66 to 2.70 k Ω at 300 K was observed, while during the same time, the resistance of a non-exposed insulating channel decreases by a few %. Additionally, a small increase of T_c was noted, from 1.91 K to 1.96 K. These observations indicate that the exposed channel is not reverting to the non-exposed insulating state. Note that for samples kept at lower temperature (-30°C), no significant evolution was observed. This room temperature stability rules out a surface-limited mechanism driven by oxygen exchange between the film and the atmosphere. Mechanisms not involving oxygen outdiffusion which can affect the bulk of the films have been previously discussed in a- InO_x films [26]. If a photon causes an electron transfer from O^{2-} to In^{3+} ion, the resulting O^- ion may form weak covalent bonds with a neighboring O^{2-} ion or stronger bonds with another O^- ion. This process increases the electron concentration, leading to higher charge carrier density and electrical conductance.

Another important question pertains to how the $R_{\square} - T$ curves of our e-beam-exposed superconducting films compare to those obtained through the conventional method of adjusting the oxygen pressure during film deposition. We prepared a few films with thicknesses ranging from 20 to 47 nm and oxygen pressures between 0 (no added oxygen in the evaporation chamber)

and 6×10^{-5} mbar with a fixed evaporation rate of 2 Å/s. In these films, the R_{\square} value for a given thickness is determined by the amount of oxygen vacancies present [3, 30]. The highest T_c achieved in 30 nm thick films was about 1.4 K, when no O₂ was introduced during e-beam evaporation. The $R_{\square} - T$ curve of this film appears to fall between those of exposed films with T_c of 1.2 and 1.9 K (see Fig. 6). Moreover, comparing an e-beam-exposed sample and a 40 nm thick film evaporated under 3×10^{-5} mbar of O₂, both having similar $T_c \approx 1.2$ K, their $R_{\square} - T$ curves are almost identical. These results suggest that the effect of e-beam exposure is equivalent to a change in oxygen vacancies content, at least regarding the $R_{\square} - T$ dependency. Additionally, our e-beam exposure process enables achieving much higher T_c in very thin films compared with the standard evaporation process: a saturation value of ~ 2.85 K for our 30 nm thick films, compared to ~ 1.4 K in 30 nm thick unexposed films when no oxygen was added during the evaporation in our setup. However, it is worth mentioning that critical temperatures as high as 2.4 K have been achieved using different setups [46, 47, 48], while T_c up to 3.4 K can be obtained in a-InO_x films by annealing and increasing the thickness [23, 32].

Conclusion

A new technique to locally transform an insulating amorphous indium oxide film into superconducting by e-beam exposure has been proposed. The T_c values of the irradiated superconducting region can be finely tuned by adjusting the acceleration voltage and electron dose, achieving a maximum T_c value of approximately 2.8 K in 30 nm thick films. The resulting $R_{\square} - T$ curves closely resemble those of amorphous indium oxide films deposited under different oxygen pressures.

This innovative approach to fabricating superconducting amorphous indium oxide films opens avenues for fundamental studies of the superconducting-insulating transition in this system. Typically, films made under different oxygen pressures lack precise control over R_{\square} and T_c , necessitating subsequent annealing steps. Our SEM e-beam exposure method enables fine control of electrical parameters, allowing the production of samples with varied R_{\square} and T_c values within a single SEM session and after a single evaporation step, while also ensuring same-batch sample-to-sample reproducibility.

Moreover, the resolution achieved is approximately ~ 2 μm, enabling the creation of superconducting lines just a few micrometers wide, with well-defined T_c or with micrometer-scale changes in T_c , within an insulating matrix of amorphous indium oxide. These characteristics hold promise for various applications, such as the development of high kinetic inductances or superconducting nanowire single-photon detectors.

The observed resistance changes may be related to the photoreduction of the films by X-rays and/or UV radiation emitted during e-beam interactions with the film and its substrate. Further detailed structural and chemical investigations are required to elucidate this aspect. The relaxation of these materials at room temperature remains an open question, and its study could provide valuable insight into the mechanisms underlying this behaviour.

Data availability

Data supporting the findings of this study are included within the article. The raw data underlying the results can be made available upon reasonable request. Requests for data should be directed to I. F. Llovo or J. Delahaye.

References

1. Ovadyahu, Z., Moehlecke, S. & Imry, Y. Weak localization in indium oxide films. *Surf. Sci.* **113**, 544–549, DOI: [https://dx.doi.org/10.1016/0039-6028\(82\)90648-3](https://dx.doi.org/10.1016/0039-6028(82)90648-3) (1982).
2. Imry, Y. & Ovadyahu, Z. Density-of-states anomalies in a disordered conductor: A tunneling study. *Phys. Rev. Lett.* **49**, 841–844, DOI: <https://dx.doi.org/10.1103/PhysRevLett.49.841> (1982).
3. Ovadyahu, Z. Some finite temperature aspects of the Anderson transition. *J. Phys. C* **19**, 5187, DOI: <https://dx.doi.org/10.1088/0022-3719/19/26/018> (1986).
4. Davies, J. H., Lee, P. A. & Rice, T. M. Electron glass. *Phys. Rev. Lett.* **49**, 758–761, DOI: <https://dx.doi.org/10.1103/PhysRevLett.49.758> (1982).
5. Grunewald, M., Pohlmann, B., Schweitzer, L. & Wurtz, D. Mean field approach to the electron glass. *J. Phys. C* **15**, L1153, DOI: <https://dx.doi.org/10.1088/0022-3719/15/32/007> (1982).
6. Pollak, M. & Ortuño, M. Coulomb interactions in Anderson localized disordered systems. *Sol. Energy Mater.* **8**, 81–89, DOI: [https://dx.doi.org/10.1016/0165-1633\(82\)90052-1](https://dx.doi.org/10.1016/0165-1633(82)90052-1) (1982).
7. Ben-Chorin, M., Ovadyahu, Z. & Pollak, M. Nonequilibrium transport and slow relaxation in hopping conductivity. *Phys. Rev. B* **48**, 15025–15034, DOI: <https://dx.doi.org/10.1103/PhysRevB.48.15025> (1993).
8. Vaknin, A., Ovadyahu, Z. & Pollak, M. Nonequilibrium field effect and memory in the electron glass. *Phys. Rev. B* **65**, 134208, DOI: <https://dx.doi.org/10.1103/PhysRevB.65.134208> (2002).

9. Pollak, M., Ortuño, M. & Frydman, A. *The Electron Glass* (Cambridge University Press, Cambridge, 2012).
10. Hebard, A. F. & Paalanen, M. A. Magnetic-field-tuned superconductor-insulator transition in two-dimensional films. *Phys. Rev. Lett.* **65**, 927–930, DOI: <https://dx.doi.org/10.1103/PhysRevLett.65.927> (1990).
11. Gantmakher, V. F., Golubkov, M. V., Dolgoplov, V. T., Tsydynzhapov, G. E. & Shashkin, A. A. Scaling analysis of the magnetic field-tuned quantum transition in superconducting amorphous In-O films. *JETP Lett.* **71**, 160–164, DOI: <https://dx.doi.org/10.1134/1.568304> (2000).
12. Sambandamurthy, G., Engel, L. W., Johansson, A. & Shahar, D. Superconductivity-related insulating behavior. *Phys. Rev. Lett.* **92**, 107005, DOI: <https://dx.doi.org/10.1103/PhysRevLett.92.107005> (2004).
13. Shahar, D. & Ovadyahu, Z. Superconductivity near the mobility edge. *Phys. Rev. B* **46**, 10917–10922, DOI: <https://dx.doi.org/10.1103/PhysRevB.46.10917> (1992).
14. Sambandamurthy, G., Engel, L. W., Johansson, A., Peled, E. & Shahar, D. Experimental evidence for a collective insulating state in two-dimensional superconductors. *Phys. Rev. Lett.* **94**, 017003, DOI: <https://dx.doi.org/10.1103/PhysRevLett.94.017003> (2005).
15. Sacépé, B., Feigel'man, M. & Klapwijk, T. M. Quantum breakdown of superconductivity in low-dimensional materials. *Nat. Phys.* **16**, 734–746, DOI: <https://dx.doi.org/10.1038/s41567-020-0905-x> (2020).
16. Ovadia, M. *et al.* Evidence for a finite-temperature insulator. *Sci. Rep.* **5**, 13503, DOI: <https://dx.doi.org/10.1038/srep13503> (2015).
17. Gornyi, I. V., Mirlin, A. D. & Polyakov, D. G. Interacting electrons in disordered wires: Anderson localization and low-*T* transport. *Phys. Rev. Lett.* **95**, 206603, DOI: <https://dx.doi.org/10.1103/PhysRevLett.95.206603> (2005).
18. Basko, D., Aleiner, I. & Altshuler, B. Metal–insulator transition in a weakly interacting many-electron system with localized single-particle states. *Ann. Phys.* **321**, 1126–1205, DOI: <https://dx.doi.org/https://doi.org/10.1016/j.aop.2005.11.014> (2006).
19. Oganesyan, V. & Huse, D. A. Localization of interacting fermions at high temperature. *Phys. Rev. B* **75**, 155111, DOI: <https://dx.doi.org/10.1103/PhysRevB.75.155111> (2007).
20. Nandkishore, R. & Huse, D. A. Many-body localization and thermalization in quantum statistical mechanics. *Annu. Rev. Condens. Matter Phys.* **6**, 15–38, DOI: <https://dx.doi.org/10.1146/annurev-conmatphys-031214-014726> (2015).
21. Alet, F. & Laflorencie, N. Many-body localization: an introduction and selected topics. *C. R. Phys.* **19**, 498–525, DOI: <https://dx.doi.org/10.1016/j.crhy.2018.03.003> (2018).
22. Astafiev, O. V. *et al.* Coherent quantum phase slip. *Nature* **484**, 355–358, DOI: <https://dx.doi.org/10.1038/nature10930> (2012).
23. Charpentier, T. *et al.* First-order quantum breakdown of superconductivity in an amorphous superconductor. *Nat. Phys.* **21**, 104–109, DOI: [10.1038/s41567-024-02713-8](https://dx.doi.org/10.1038/s41567-024-02713-8) (2025).
24. Dupré, O. *et al.* Tunable sub-gap radiation detection with superconducting resonators. *Supercond. Sci. Technol.* **30**, 045007, DOI: <https://dx.doi.org/10.1088/1361-6668/aa5b14> (2017).
25. Bellingham, J., Phillips, W. & Adkins, C. Amorphous indium oxide. *Thin Solid Films* **195**, 23–32, DOI: [https://dx.doi.org/10.1016/0040-6090\(91\)90255-V](https://dx.doi.org/10.1016/0040-6090(91)90255-V) (1991).
26. Pashmakov, B., Claflin, B. & Fritzsche, H. Transport near the mobility edge, the sign of the hall effect, photoreduction and oxidation of amorphous InO_x. *J. Non-Cryst. Solids* **164–166**, 441–444, DOI: [https://dx.doi.org/10.1016/0022-3093\(93\)90584-K](https://dx.doi.org/10.1016/0022-3093(93)90584-K) (1993). Proceedings of the Fifteenth International Conference on Amorphous Semiconductors – Science and Technology.
27. Pashmakov, B., Claflin, B. & Fritzsche, H. Photoreduction and oxidation of amorphous indium oxide. *Solid State Commun.* **86**, 619–622, DOI: [https://dx.doi.org/10.1016/0038-1098\(93\)90826-9](https://dx.doi.org/10.1016/0038-1098(93)90826-9) (1993).
28. Fritzsche, H., Pashmakov, B. & Claflin, B. Reversible changes of the optical and electrical properties of amorphous InO_x by photoreduction and oxidation. *Sol. Energy Mater. Sol. Cells* **32**, 383–393, DOI: [https://dx.doi.org/10.1016/0927-0248\(94\)90101-5](https://dx.doi.org/10.1016/0927-0248(94)90101-5) (1994). Special Issue Dedicated to Professor Bernhard Seraphin.
29. Claflin, B. & Fritzsche, H. The role of oxygen diffusion in photoinduced changes of the electronic and optical properties in amorphous indium oxide. *J. Electron. Mater.* **25**, 1772–1777, DOI: <https://dx.doi.org/10.1007/s11664-996-0034-z> (1996).
30. Givan, U. & Ovadyahu, Z. Compositional disorder and transport peculiarities in the amorphous indium oxides. *Phys. Rev. B* **86**, 165101, DOI: <https://dx.doi.org/10.1103/PhysRevB.86.165101> (2012).
31. Dawar, A. L. & Joshi, J. C. Semiconducting transparent thin films: their properties and applications. *J. Mater. Sci.* **19**, 1–23, DOI: <https://dx.doi.org/10.1007/BF02403106> (1984).
32. Sacépé, B. *et al.* High-field termination of a Cooper-pair insulator. *Phys. Rev. B* **91**, 220508(R), DOI: <https://dx.doi.org/10.1103/PhysRevB.91.220508> (2015).
33. Ovadyahu, Z. Slow dynamics of electron glasses: The role of disorder. *Phys. Rev. B* **95**, 134203, DOI: <https://dx.doi.org/10.1103/PhysRevB.95.134203> (2017).
34. Ovadyahu, Z. Structural dynamics in thermal treatment of amorphous indium oxide films. *Phys. Status Solidi B* **257**,

- 1900310, DOI: <https://dx.doi.org/10.1002/pssb.201900310> (2020).
35. Ovadyahu, Z. Memory versus irreversibility in the thermal densification of amorphous glasses. *Phys. Rev. B* **95**, 214207, DOI: <https://dx.doi.org/10.1103/PhysRevB.95.214207> (2017).
 36. Reimer, L. *Scanning Electron Microscopy: Physics of Image Formation and Microanalysis*. Optical Sciences (Springer, Berlin, 1998).
 37. Wang, Z. *et al.* Measurement and evaluation of local surface temperature induced by irradiation of nanoscaled or microscaled electron beams. *Nanoscale Res. Lett.* **14**, 31, DOI: <https://dx.doi.org/10.1186/s11671-018-2821-x> (2019).
 38. Drouin, D. *et al.* CASINO V2.42 – A fast and easy-to-use modeling tool for scanning electron microscopy and microanalysis users. *Scanning* **29**, 92–101, DOI: <https://dx.doi.org/10.1002/sca.20000> (2007).
 39. Kern, P., Jäggi, C., Utke, I., Friedli, V. & Michler, J. Local electron beam induced reduction and crystallization of amorphous titania films. *Appl. Phys. Lett.* **89**, 021902, DOI: [10.1063/1.2219398](https://doi.org/10.1063/1.2219398) (2006). https://pubs.aip.org/aip/apl/article-pdf/doi/10.1063/1.2219398/14353380/021902_1_online.pdf.
 40. Kern, P., Müller, Y., Patscheider, J. & Michler, J. Electron-beam-induced topographical, chemical, and structural patterning of amorphous titanium oxide films. *The J. Phys. Chem. B* **110**, 23660–23668, DOI: [10.1021/jp0642589](https://doi.org/10.1021/jp0642589) (2006).
 41. Zhang, Y. *et al.* Artificially controlled nanoscale chemical reduction in vo2 through electron beam illumination. *Nat. Commun.* **14**, 4012, DOI: [10.1038/s41467-023-39812-8](https://doi.org/10.1038/s41467-023-39812-8) (2023).
 42. Zhang, Y., Zhang, F., Li, L. & Yu, P. Artificially controlled nanoscale chemical reduction via electron beam illumination. *Microsc. Microanal.* **30**, ozae044.538, DOI: [10.1093/mam/ozae044.538](https://doi.org/10.1093/mam/ozae044.538) (2024). https://academic.oup.com/mam/article-pdf/30/Supplement_1/ozae044.538/58671848/ozae044.538.pdf.
 43. Lo Mastro, A., Tringali, F., Miritello, M., Franzò, G. & Terrasi, A. Intrinsic doping and ageing of indium oxide thin films. *Appl. Surf. Sci.* **670**, 160716, DOI: <https://doi.org/10.1016/j.apsusc.2024.160716> (2024).
 44. Korotcenkov, G., Nazarov, M., Zamoryanskaya, M. & Ivanov, M. Cathodoluminescence emission study of nanocrystalline indium oxide films deposited by spray pyrolysis. *Thin Solid Films* **515**, 8065–8071, DOI: <https://doi.org/10.1016/j.tsf.2007.03.186> (2007).
 45. Maestre, D., Cremades, A., Piqueras, J. & Gregoratti, L. Thermal growth and structural and optical characterization of indium tin oxide nanopillars, nanoislands, and tubes. *J. Appl. Phys.* **103**, 093531, DOI: [10.1063/1.2919770](https://doi.org/10.1063/1.2919770) (2008). https://pubs.aip.org/aip/jap/article-pdf/doi/10.1063/1.2919770/15015726/093531_1_online.pdf.
 46. Crane, R. *et al.* Survival of superconducting correlations across the two-dimensional superconductor-insulator transition: A finite-frequency study. *Phys. Rev. B* **75**, 184530, DOI: [10.1103/PhysRevB.75.184530](https://doi.org/10.1103/PhysRevB.75.184530) (2007).
 47. Liu, W. *et al.* Microwave spectroscopy evidence of superconducting pairing in the magnetic-field-induced metallic state of InO_x films at zero temperature. *Phys. Rev. Lett.* **111**, 067003, DOI: [10.1103/PhysRevLett.111.067003](https://doi.org/10.1103/PhysRevLett.111.067003) (2013).
 48. Wang, Y., Tamir, I., Shahar, D. & Armitage, N. P. Absence of cyclotron resonance in the anomalous metallic phase in InO_x . *Phys. Rev. Lett.* **120**, 167002, DOI: [10.1103/PhysRevLett.120.167002](https://doi.org/10.1103/PhysRevLett.120.167002) (2018).

Acknowledgements

The authors would like to thank Dr. T. Grenet and Prof. M. V. Ramallo for their invaluable insight during our conversations on the topic. I. F. Llovo acknowledges financial support from Xunta de Galicia through grant ED481A-2020/149. J. Delahaye acknowledges financial support from the Agence Nationale de la Recherche (grant ANR-19-CE30-0014-04).

Author contributions

Both authors contributed to the conceptualization of the study, experimental work, analysis and writing of the manuscript.

Competing interests

The authors declare no competing interests.